

Driving corrugated donut rotors with Laguerre-Gauss beams

Vincent L. Y. Loke,¹ Theodor Asavei,² Alexander B. Stilgoe,¹
Timo A. Nieminen,^{1,*} and Halina Rubinsztein-Dunlop¹

¹The University of Queensland, Quantum Science Laboratory, School of Mathematics and Physics, Brisbane, QLD 4072, Australia

²ELI-NP Centre, Magurele, Romania

*loke@physics.uq.edu.au

Abstract: Tightly-focused laser beams that carry angular momentum have been used to trap and rotate microrotors. In particular, a Laguerre-Gauss mode laser beam can be used to transfer its orbital angular momentum to drive microrotors. We increase the torque efficiency by a factor of about 2 by designing the rotor such that its geometry is compatible with the driving beam, when driving the rotation with the optimum beam, rather than beams of higher or lower orbital angular momentum. Based on Floquet's theorem, the order of discrete rotational symmetry of the rotor can be made to couple with the azimuthal mode of the Laguerre-Gauss beam. We design corrugated donut rotors, that have a flat disc-like profile, with the help of the discrete dipole approximation and the T-matrix methods in parallel with experimental demonstrations of stable trapping and torque measurement. We produce and test such a rotor using two-photon photopolymerization. With a rotor that has 8-fold discrete rotational symmetry, an outer radius of $1.85 \mu\text{m}$ and a hollow core radius of $0.5 \mu\text{m}$, we were able to transfer approximately $0.3 \hbar$ per photon of the orbital angular momentum from an LG₀₄ beam.

© 2014 Optical Society of America

OCIS codes: (220.4000) Microstructure fabrication; (230.3990) Micro-optical devices; (350.4855) Optical tweezers or optical manipulation.

References and links

1. P. Galajda and P. Ormos, "Complex micromachines produced and driven by light," *Appl. Phys. Lett.* **78**, 249–251 (2001).
2. S. Maruo, A. Takaura, and Y. Saito, "Optically driven micropump with a twin spiral microrotor," *Opt. Express* **17**, 18525–18532 (2009).
3. T. Asavei, T. A. Nieminen, V. L. Y. Loke, A. B. Stilgoe, R. Bowman, D. Preece, M. J. Padgett, N. R. Heckenberg, and H. Rubinsztein-Dunlop, "Optically trapped and driven paddle-wheel," *New J. Phys.* **15**, 063016 (2013).
4. M. E. J. Friese, T. A. Nieminen, N. Heckenberg, and H. Rubinsztein-Dunlop, "Optical alignment and spinning of laser-trapped microscopic particles," *Nature* **394**, 348–350 (1998). Erratum: *Nature* **395**, 621 (1998).
5. S. J. Parkin, R. Vogel, M. Persson, M. Funk, V. L. Y. Loke, T. A. Nieminen, N. R. Heckenberg, and H. Rubinsztein-Dunlop, "Highly birefringent vaterite microspheres: production, characterization and applications for optical micromanipulation," *Opt. Express* **17**, 21944–21955 (2009).
6. A. I. Bishop, T. A. Nieminen, N. R. Heckenberg, and H. Rubinsztein-Dunlop, "Optical application and measurement of torque on microparticles of isotropic nonabsorbing material," *Phys. Rev. A* **68**, 033802 (2003).
7. T. Asavei, V. L. Y. Loke, M. Barbieri, T. A. Nieminen, N. R. Heckenberg, and H. Rubinsztein-Dunlop, "Optical angular momentum transfer to microrotors fabricated by two-photon photopolymerization," *New J. Phys.* **11**, 093021 (2009).

8. C.-L. Lin, G. Vitrant, M. Bouriau, R. Casalegno, and P. L. Baldeck, "Optically driven Archimedes micro-screws for micropump application," *Opt. Express* **19**, 8267–8276 (2011).
9. H. He, N. R. Heckenberg, and H. Rubinsztein-Dunlop, "Optical-particle trapping with higher-order doughnut beams produced using high-efficiency computer-generated holograms," *J. Mod. Opt.* **42**, 217–223 (1995).
10. T. Asavei, T. A. Nieminen, N. R. Heckenberg, and H. Rubinsztein-Dunlop, "Fabrication of micro-structures for optically driven micromachines using two-photon photopolymerization of UV curing resins," *J. Opt. A* **11**, 034001 (2009).
11. H. DeVoe, "Optical properties of molecular aggregates. I. Classical model of electronic absorption and refraction," *J. Chem. Phys.* **41**, 393–400 (1964).
12. E. Purcell and C. Pennypacker, "Scattering and absorption of light by nonspherical dielectric grains," *Astrophys. J.* **186**, 705–714 (1973).
13. B. T. Draine and P. J. Flatau, "Discrete-dipole approximation for scattering calculations," *J. Opt. Soc. Am. A* **11**, 1491–1499 (1994).
14. V. L. Y. Loke, T. A. Nieminen, N. R. Heckenberg, and H. Rubinsztein-Dunlop, "T-matrix calculation via discrete-dipole approximation, point matching and exploiting symmetry," *J. Quant. Spectrosc. Radiat. Transfer* **110**, 1460–1471 (2009).
15. T. A. Nieminen, V. L. Y. Loke, A. B. Stilgoe, G. Knöner, A. M. Brańczyk, N. R. Heckenberg, and H. Rubinsztein-Dunlop, "Optical tweezers computational toolbox," *J. Opt. A* **9**, S196–S203 (2007).
16. L. Allen, M. W. Beijersbergen, R. J. C. Spreeuw, and J. P. Woerdman, "Orbital angular-momentum of light and the transformation of Laguerre-Gaussian laser modes," *Phys. Rev. A* **45**, 8185–8189 (1992).
17. N. R. Heckenberg, R. McDuff, C. P. Smith, and A. G. White, "Generation of optical-phase singularities by computer-generated holograms," *Opt. Lett.* **17**, 221–223 (1992).
18. P. S. J. Russell, "Coupled wave versus modal theory in uniform dielectric gratings," *Opt. Commun.* **48**, 71–74 (1983).
19. K. P. Huy, A. Morand, and P. Benech, "Modelization of the whispering gallery mode in microgear resonators using the Floquet-Bloch formalism," *IEEE J. Quantum. Electron.* **41**, 357–365 (2005).
20. T. A. Nieminen, T. Asavei, V. L. Y. Loke, N. R. Heckenberg, and H. Rubinsztein-Dunlop, "Symmetry and the generation and measurement of optical torque," *J. Quant. Spectrosc. Radiat. Transfer* **110**, 1472–1482 (2009).
21. K. Sueda, G. Miyaji, N. Miyanaga, and M. Nakatsuka, "Laguerre-Gaussian beam generated with a multilevel spiral phase plate for high intensity laser pulses," *Opt. Express* **12**, 3548–3553 (2004).
22. G. Knöner, S. Parkin, T. A. Nieminen, V. L. Y. Loke, N. R. Heckenberg, and H. Rubinsztein-Dunlop, "Integrated optomechanical microelements," *Opt. Express* **15**, 5521–5530 (2007).
23. H. Rubinsztein-Dunlop, T. Asavei, A. B. Stilgoe, V. L. Y. Loke, R. Vogel, T. A. Nieminen, and N. R. Heckenberg, "Design of optically driven microrotors," in *Optical Nano and Micro Actuator Technology*, G. K. Knopf and Y. Otani, eds. (CRC Press, 2012), pp. 277–306.
24. S. J. W. Parkin, G. Knöner, T. A. Nieminen, N. R. Heckenberg, and H. Rubinsztein-Dunlop, "Measurement of the total optical angular momentum transfer in optical tweezers," *Opt. Express* **14**, 6963–6970 (2006).
25. R. C. Gauthier, "Computation of the optical trapping force using an FDTD based technique," *Opt. Express* **13**, 3707–3718 (2005).
26. D. A. White, "Vector finite element modeling of optical tweezers," *Comput. Phys. Commun.* **128**, 558–564 (2000).
27. T. A. Nieminen, V. L. Y. Loke, A. B. Stilgoe, N. R. Heckenberg, and H. Rubinsztein-Dunlop, "T-matrix method for modelling optical tweezers," *J. Mod. Opt.* **58**, 528–544 (2011).
28. B. T. Draine and J. Goodman, "Beyond Clausius–Mossotti: wave propagation on a polarizable point lattice and the discrete dipole approximation," *Astrophys. J.* **405**, 685–697 (1993).
29. V. L. Y. Loke, M. P. Mengüç, and T. A. Nieminen, "Discrete dipole approximation with surface interaction: Computational toolbox for MATLAB," *J. Quant. Spectrosc. Radiat. Transfer* **112**, 1711–1725 (2011).
30. T. A. Nieminen, N. R. Heckenberg, and H. Rubinsztein-Dunlop, "Multipole expansion of strongly focussed laser beams," *J. Quant. Spectrosc. Radiat. Transfer* **79–80**, 1005–1017 (2003).
31. M. I. Mischenko, J. W. Hovenier, and L. D. Travis, *Light Scattering by Nonspherical Particles: Theory, Measurements and Applications* (Academic, 2000).
32. B. Brock, "Using vector spherical harmonics to compute antenna mutual impedance from measured or computed fields," Tech. Rep. SAND2000-2217-Revised, Sandia National Laboratories, Albuquerque, NM (2001).
33. Ø. Farsund and B. U. Felderhof, "Force, torque, and absorbed energy for a body of arbitrary shape and constitution in an electromagnetic radiation field," *Physica A* **227**, 108–130 (1996).
34. T. A. Nieminen, N. R. Heckenberg, and H. Rubinsztein-Dunlop, "Calculation of the T-matrix: general considerations and application of the point-matching method," *J. Quant. Spectrosc. Radiat. Transfer* **79–80**, 1019–1029 (2003).

1. Introduction

An optically-driven microrotor can be used as a component of micromachines where it can act as an impeller for a pump, an agitator for a mixing chamber, a probe for viscosity measurements as well as being used in many other applications in the microfluidic regime [1–3]. The microrotor can acquire torque from a trapping and driving beam via spin angular momentum transfer due to its birefringence (material [4, 5] or structural form [6]) or orbital angular momentum (OAM) transfer due to azimuthal mode coupling with its structure. In the latter case, torque may be imparted on the rotor either from an incident beam carrying OAM [7] or, if the beam does not carry OAM, via asymmetric reflection from rotor’s chiral structure [1, 8]. All these factors contribute to the torque. In this paper, we focus on orbital angular momentum transfer due to the coupling between the specific geometry of a structure to specific modes of the beam carrying OAM. (The materials that we use to fabricate the microrotors are non-absorbing. Otherwise, OAM transfer may also occur via absorption [9]).

It has been demonstrated that a tightly-focused Laguerre-Gauss (LG) beam can be used to trap and spin a microrotor with discrete rotational symmetry [10] where the rotor had a 4-fold discrete rotational symmetry and where its stalk coincided with the rotational axis. Motivated by foreseeable dimensional constraints, e.g., the need for a flat disc-like rotor, we design a donut-shaped rotor with 8-fold discrete rotational symmetry, which we call a corrugated donut rotor (CDR). We perform optical micromanipulation experiments with the rotor shown in Fig. 1, fabricated by two-photon photopolymerization in parallel with computational modeling for calculating forces and torques, thereby minimizing the trial-and-error approach in the design process.

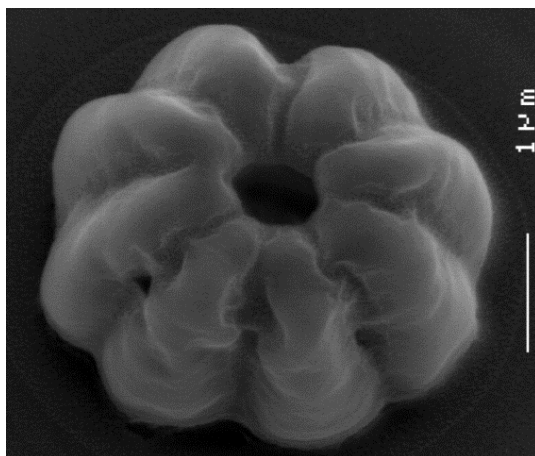


Fig. 1. Corrugated donut rotor with 8-fold discrete rotational symmetry fabricated by two-photon photopolymerization. Some deformation resulted in the “ring cake” shape. The visible layers stem from layer-by-layer printing of individual voxels.

The discrete dipole approximation [11–13] (DDA) is our method of choice, for calculations of forces and torques on the rotor, due to its accuracy in modeling the interaction of light with scatterers of arbitrary shapes. Because of the need to perform repeated force and torque calculations when the relative position of the rotor and the illumination changes, we use DDA to calculate the T-matrix [14] which facilitates rapid calculations of the scattered field and the optical force and torque [15].

2. Laguerre-Gauss beams

The Laguerre-Gauss laser beam is represented by the notation, LG_{pl} , where p and l are the radial and azimuthal mode indices. Apart from LG_{00} , which is a Gaussian beam, LG_{0l} beams, where $l \neq 0$, are often called “donut” beams due to the phase singularity at its core, which appears as a zero-intensity dark spot. The radial mode index p determines the number of concentric rings the beam has, whereas l determines the azimuthal angular dependence ($\exp(il\phi)$) of the amplitude within the ring. The OAM carried by an LG_{0l} beam is well defined [16] and is $l\hbar$ angular momentum per photon. The phase structure of an LG beam resembles azimuthally periodic helical wavefronts; the number of helices is equal to the azimuthal mode index (Fig. 2).

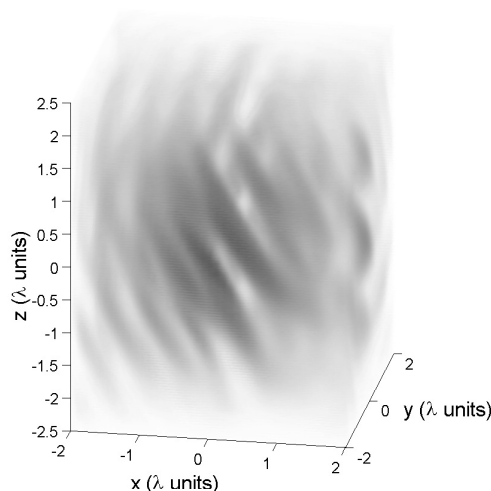


Fig. 2. A rendering of the instantaneous field intensity of an LG_{04} beam (convergence angle $\theta = 78^\circ$) with azimuthally periodic wavefronts where the phase structures are made up of four helices.

We produce LG beams using computer-generated holograms [9, 17]. Holograms for the $LG_{0,\pm 4}$ and $LG_{0,\pm 8}$ modes are shown in Figs. 3 and 4 respectively. The $\exp(il\phi)$ periodicity is obvious for on-axis holograms. On the other hand, the off-axis hologram is produced by superimposing a periodic linear grating function with $\exp(il\phi)$. With the off-axis hologram, different modes are deviated off axis, laterally, at specific angles; selection of the required mode can be made by simply screening off the unwanted modes. The on-axis hologram, which will produce two superposed beams of opposite handedness is not useful for generating orbital angular momentum from an incident Gaussian beam. However, it provides a suitable picture of the function of the CDR.

3. Corrugated donut rotor

The symmetry of the microrotor is studied and exploited to optimize the torque when driven with an LG beam. We have demonstrated that a stalk and 4-arm design can be stably trapped and rotated [10]. However, potential spatial constraints may favor a flatter structure. We also expect that the flatness of the CDR, as opposed to the rotor with a long stalk, is better suited for fabrication using micro- or nano-lithographic methods. Thus, we design the CDR where the structure is compatible with the LG ring and its order of discrete rotational symmetry is

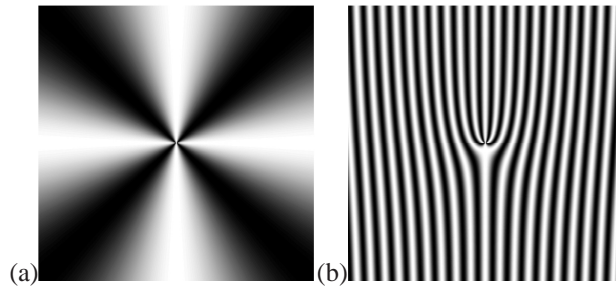


Fig. 3. (a) On-axis and (b) off-axis holograms for generating $LG_{0,4}$ and $LG_{0,-4}$ modes.

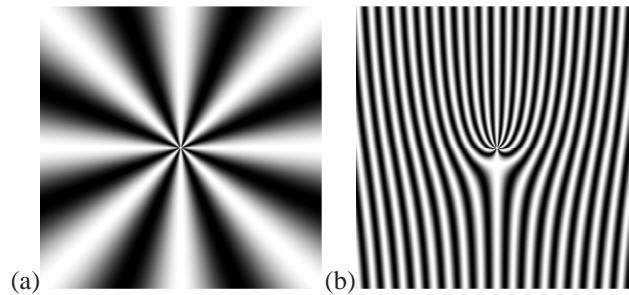


Fig. 4. (a) On-axis and (b) off-axis holograms for generating $LG_{0,8}$ and $LG_{0,-8}$ modes.

intended to achieve coupling between the incident LG and scattered azimuthal modes.

The CDRs themselves can be regarded as holograms in that they change the phase structure of the incident beam. The equivalent holograms for blazed (sawtooth) and sinusoidal CDRs are shown in Figs. 5(a) and 5(b), respectively; in contrast to the LG_{08} on-axis hologram in Fig. 4(a), the CDR hologram equivalents are ring-shaped and have hollow cores.

When a CDR with q -fold discrete rotational symmetry is trapped with an LG_{0l} beam, the scattered modes will be $l_j = l_0 + jq$, where l_0 is the azimuthal mode of the incident beam and j is an integer. This is a consequence of Floquet's theorem [18] albeit working in the azimuthal direction with periodic boundary conditions [19, 20]. The incident beam carries $l_0\hbar$ OAM per photon whereas the CDR scatters into modes with $l_j\hbar$ angular momentum per photon.

Given that the CDR, in our case, has 8-fold discrete rotational symmetry, i.e., $q = 8$, if the incident beam is LG_{04} , the scattered light couples to $LG_{0,-12}$, $LG_{0,4}$ and $LG_{0,12}$. Since the LG_{04} has mode overlap, the beam is suitable for producing torque when used on a sinusoidal or triangular wave CDR.

If we use an LG_{00} beam, which carries no orbital angular momentum, the scattered modes are $LG_{0,-16}$, $LG_{0,-8}$, $LG_{0,+8}$ and $LG_{0,+16}$. That implies no net torque. However, torque can still be produced if we used a blazed CDR; due to the asymmetry of the corrugated profile, linear momentum of the beam is converted, via reflection and refraction, to the azimuthal direction. In other words, angular momentum is produced.

Beams with higher order LG_{0l} modes carry more OAM per unit power and they also have ring sizes of larger radii for a given numerical aperture. Previous designs that involve rotor arms connected to a stalk [10] on the rotational axis cannot be stably trapped on the axis of an LG beam, as most, if not all, of the rotor would sit in the low-intensity core of the beam. The intensity profile of the beam should be taken into account when designing the CDR. Ideally, the

size of the CDR ring should coincide with that of the LG beam to fully exploit the OAM of the incident beam as well as to achieve optimal stability. For stable three-dimensional trapping in an orientation where it can function as an on-axis hologram modifying the trapping and driving beam, the CDR needs to be close to the width of the LG beam in the focal region. If the CDR is wider, it will tend to “flip” in the trap, orienting with its longest dimension vertically. If the CDR is narrower, it will be trapped in one side of the ring, rather than in the center of the beam (and will also be trapped vertically). This requirement that the CDR is similar in size to the Laguerre-Gauss beam means that it must be very small. As a result, it is very unlikely that a CDR would be an optimal hologram, in the sense of converting the incident beam into a desired LG mode, which can be done efficiently with larger microfabricated holograms [21, 22], but at the cost of being much too large to trap stably or three-dimensionally in an optical trap. What we will consider the optimization of is how best to couple the CDR and the driving beam, producing the highest torque efficiency subject to the fundamental constraints imposed by the size.

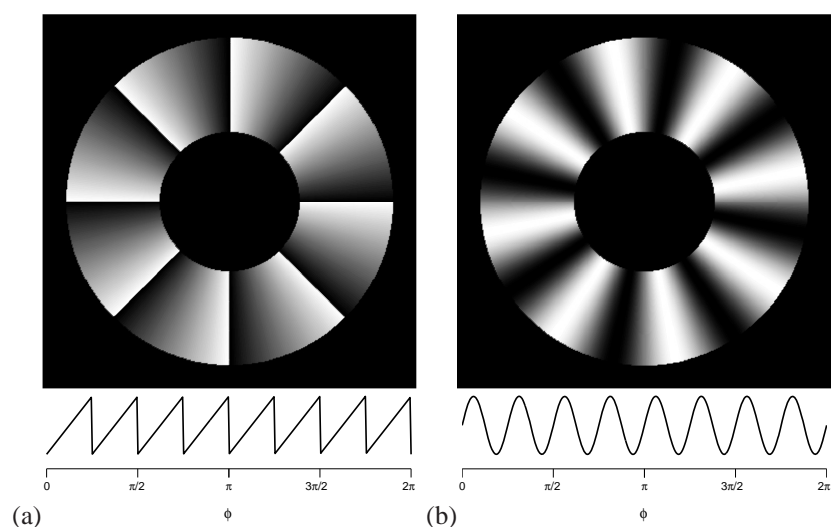


Fig. 5. The equivalent holograms for (a) blazed and (b) sinusoidal corrugated donut rotors.

4. Experiment

The experiment involves, firstly, fabricating the CDR by two-photon photopolymerization and, secondly, performing optical manipulation and torque measurements on the CDR. The experimental setup, as shown in Fig. 6, comprises components that are used in both processes: the objective lens (Olympus 100 \times , NA= 1.3), microscope slide, coverslip and stage. The femtosecond pulsed laser (Spectra Physics Tsunami pumped by Verdi, with a maximum power output of 10 W) is used for two-photon photopolymerization and the fiber laser (IPG 5 W, 1070 nm) is used for trapping and spinning the CDR. Photodetectors PD1 and PD2 are used for measuring the change in circular polarization of the transmitted beam which is collimated by a condenser. PD3 measures the rotation rate of the CDR through monitoring the intensity variations. The lamp illuminates the region of interest in the sample for video capture via a CCD camera. Details of the experimental setup are discussed in [23].

The CDR is fabricated using two-photon photopolymerization which involves 3D layer-by-layer raster scanning a UV curing resin (NOA63 from Norland Products) encapsulated within

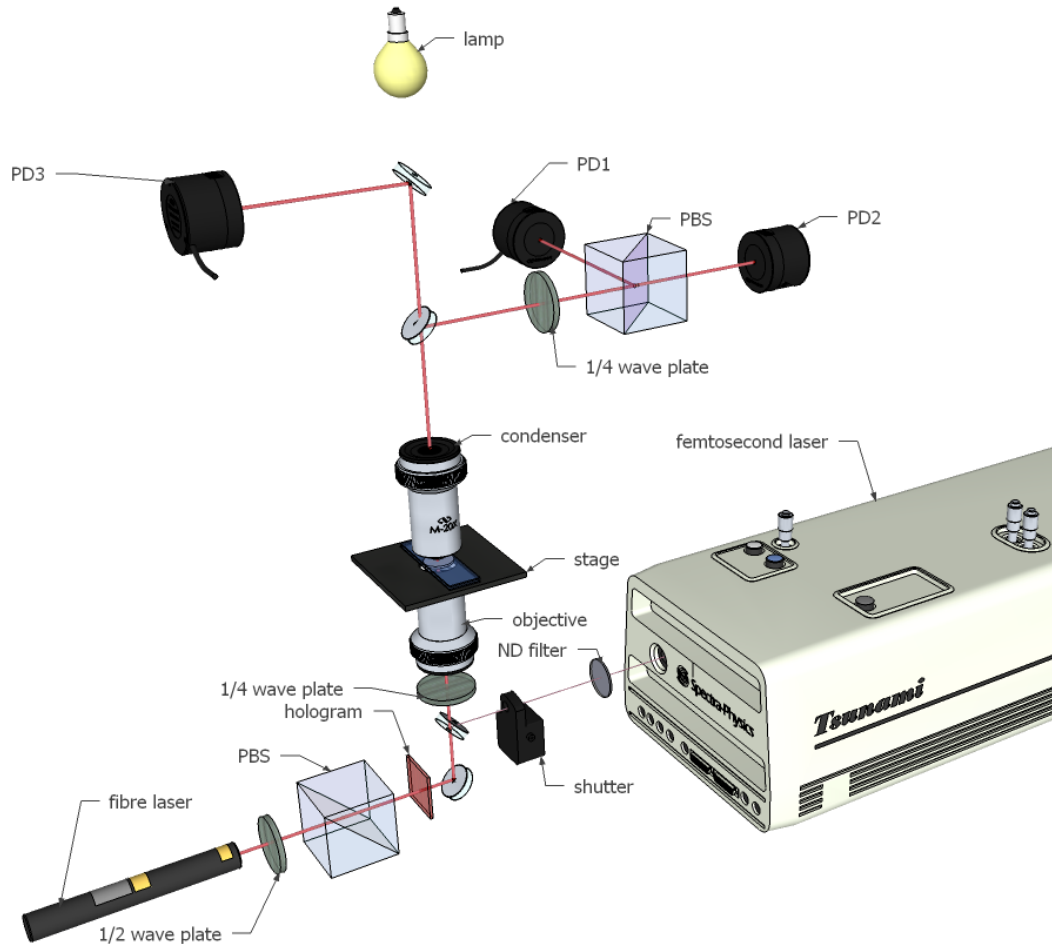


Fig. 6. Experimental setup for the two-photon photopolymerization process and optical micromanipulation. The femtosecond laser is used to cure the resin encapsulated between a microscope slide and coverslip which are placed on a piezo-controlled stage. The unpolymerized portion is washed away. The IPG fiber laser is used to trap and spin the rotor. Light transmitted through the rotor is collected in a condenser and the transmitted light is used for a measurement of the changes in the polarization of this transmitted light in comparison with the incoming light's polarization (PD1 and PD2). A small portion of the transmitted light is sent to a photodetector PD3 that enables measurement of the rotation rate of the rotor.

two microscope cover slips (Fig. 7(a)). The cover slips are placed on a computer-controlled piezo stage which moves in the x , y and z directions. Pulses from the femtosecond laser cure the resin in the vicinity of the focus – approximately 170 nm in the x and y directions and 500 nm in the z direction [3]. The uncured portion of the resin is washed away with acetone, leaving the finished product, i.e., the CDR (Fig. 1). The cover slip chamber in which the CDR sits is then filled with demineralized water. Whilst residing in a strong laser trap, the CDR is mechanically freed from the microscope slide. Details of the two-photon photopolymerization process are described in [10, 23].

Using a tightly-focused LG_{04} laser beam, the CDR is trapped and spun (Fig. 7(b)). The ro-

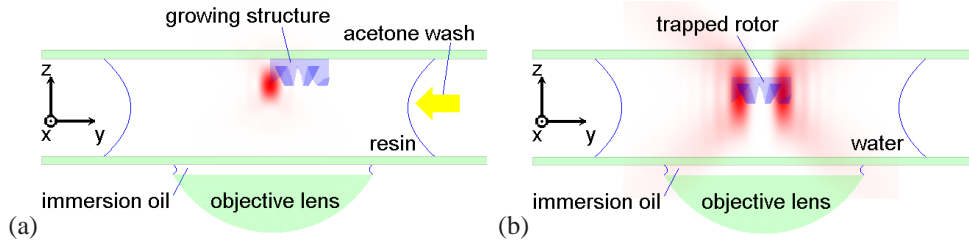


Fig. 7. Schematic diagrams of a) the two-photon photopolymerization process and b) the CDR beam trapped and rotated by the Laguerre-Gauss beam.

tation rate, measured by the intensity variation of the transmitted beam in an off-axis direction, is one quarter of the signal frequency [7]. We determine the optical torque using the method described in [24] which is based on the assumption that the total torque, τ_{total} , being the sum of the spin and orbital components,

$$\tau_{\text{total}} = \tau_{\text{spin}} + \tau_{\text{orbital}} = D\Omega, \quad (1)$$

where $D\Omega$ is the drag torque exerted on the CDR by the surrounding fluid, Ω is the angular speed, and D is constant due to the low Reynolds number regime (creeping flow; note that $\text{Re} = 2\pi\rho a^2\Omega/\eta$, where a is the radius of the CDR and η is the viscosity of the fluid, so $\text{Re} < 0.016 \ll 1$ for $a = 2\mu\text{m}$ and rotation rates of below 100 Hz). Due to the very low Reynolds number regime (creeping flow), we can assume that the CDR is rotating at its terminal angular velocity. For left-handed, right-handed and linear polarizations, the spin torque is $\tau_{\text{spin}} > 0$, $\tau_{\text{spin}} < 0$ and $\tau_{\text{spin}} = 0$, respectively. The orbital torque is assumed to be constant because the spatial structure of the the beam does not change with polarization. Thus, by performing measurements of the spin torque and rotation rates for all three polarizations, we obtain enough information to determine D , τ_{orbital} and τ_{total} . By measuring the beam power P at the focus, we determine the torque efficiency, i.e., the power independent measure of torque, $Q_{\tau} = \tau_{\text{total}}/P$.

5. Modeling methodology

5.1. Discrete dipole approximation

The discrete dipole approximation (DDA) [12, 13] method is suitable for modeling the interaction between arbitrary electric fields and an arbitrarily-shaped micron-sized objects. It is the method of choice here because the CDR has a complex shape whilst the incident field is a tightly-focused Laguerre-Gauss laser beam. In principle, other spatial discretisation schemes such as finite difference time domain (FDTD) [25] method and the finite element method (FEM) [26] can be used for force and torque calculations. However, there are challenges associated with structured light illumination, computational domain, boundary conditions and formulation of the T-matrix [27] that do not arise with DDA.

In DDA, the illuminated object is represented as a lattice of polarizable point dipoles; the model of the CDR in Fig. 8 depicts the dipoles as small spheres to show the lattice spacing. The dipoles not only respond to the incident field $\mathbf{E}_{\text{inc},j}$ but also the re-radiation from the other dipoles, thus the total field [13] at a given dipole,

$$\mathbf{E}_j = \mathbf{E}_{\text{inc},j} - \sum_{k \neq j} \mathbf{A}_{jk} \mathbf{P}_k, \quad (2)$$

where the second term is the sum of the fields due to the re-radiation from the other dipoles, \mathbf{A}_{jk} is the Green tensor [13] and \mathbf{P}_j is the dipole moment. Further discussion about the incident field will be covered in section 5.2.

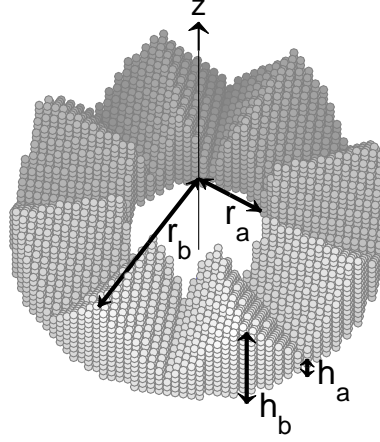


Fig. 8. Dipole lattice model of the corrugated donut rotor, designed to spin about the beam axis (shown here as the z-axis). The dimensions of the CDR are defined by the inner radius r_a , outer radius r_b , trough height h_a and peak height h_b .

The polarizability of a dipole α_j is related to the refractive index of the bulk material [28]; for a given field at the dipole, the moment is $\mathbf{P}_j = \alpha_j \mathbf{E}_j$ and by substituting \mathbf{E}_j , Eq. (2) becomes

$$\sum_{j=1}^N \mathbf{A}_{jk} \mathbf{P}_j = \mathbf{E}_{inc,k}, \quad (3)$$

from which we obtain the system of linear equations, $\mathbf{A}\mathbf{P} = \mathbf{E}_{inc}$, where the diagonal of \mathbf{A} is the inverse polarizability α^{-1} and \mathbf{P} are the unknown dipole moments to be solved, usually with a suitable iterative method (the details are outlined in [29]).

5.2. Incident and scattered fields

In many DDA implementations, a simple plane wave is used as the incident field. For optical micromanipulation, we use tightly-focused and structured laser beams, e.g., Laguerre-Gauss beams focused by lenses with numerical apertures up to $NA=1.3$. To simulate such beams, we calculate the incident field at each dipole using the vector spherical wave function (VSWF) expansion [30],

$$\mathbf{E}_{inc} = \sum_{n=1}^{N_{max}} \sum_{m=-n}^n a_{nm} \mathbf{M}_{nm}^{(3)}(k\mathbf{r}) + b_{nm} \mathbf{N}_{nm}^{(3)}(k\mathbf{r}), \quad (4)$$

where k is the wave number in the medium, \mathbf{r} is the dipole position in spherical coordinates, n is the radial mode index, m is the azimuthal mode index and $\mathbf{M}_{nm}^{(3)}$ and $\mathbf{N}_{nm}^{(3)}$ are regular VSWFs [30, 31] of the incident field; a_{nm} and b_{nm} are incident coefficients for the illuminating beam calculated using incident beam functions from [15]. We truncate the series at $N_{max} = ka + 3\sqrt[3]{ka}$ based on the criterion by [32] which defines the limit of significant terms, where a is the maximum radial extent of the region of interest, in this case, the object.

Once the solution for the dipole moments is obtained, the scattered field can be calculated for any point in the space around the object, be it in the near or in the far field zone. This is

done by essentially summing the contribution from every dipole, much like the second term in Eq. (2), for a given evaluation point r in space [29],

$$\mathbf{E}_{\text{sca}}(\mathbf{r}) = \sum_{j=1}^N \frac{\exp(ikr)}{r} \left[k^2(\hat{r}\hat{r} - \mathbf{I}_3) + \frac{ikr - 1}{r^2}(3\hat{r}\hat{r} - \mathbf{I}_3) \right] \cdot \mathbf{P}_j. \quad (5)$$

The second term is dependent on $1/r^3$ and thus rapidly becomes insignificant as we approach the far field zone.

Similar to Eq. (4), the scattered field is represented as the following VSWF expansion,

$$\mathbf{E}_{\text{sca}} = \sum_{n=1}^{N_{\text{max}}} \sum_{m=-n}^n p_{nm} \mathbf{M}_{nm}^{(1)}(kr) + q_{nm} \mathbf{N}_{nm}^{(1)}(kr), \quad (6)$$

where $\mathbf{M}_{nm}^{(1)}$ and $\mathbf{N}_{nm}^{(1)}$ are the VSWFs of the scattered field; p_{nm} and q_{nm} are the scattering coefficients. Equipped with both means of calculating the scattered field, i.e., Eqs. (5) and (6), we can proceed with calculating the T-matrix.

5.3. The T-matrix

When optimizing the design of a microrotor we have to perform many calculations where the beam parameters and relative position of the rotor changes. The purpose of the T-matrix is to expedite calculations as it needs to be calculated only once, for a given wavelength of the incident beam. The T-matrix connects the incident coefficients with those of the scattered light, by

$$\begin{bmatrix} \mathbf{p} \\ \mathbf{q} \end{bmatrix} = \mathbf{T} \begin{bmatrix} \mathbf{a} \\ \mathbf{b} \end{bmatrix}, \quad (7)$$

where the coefficients for all the associated mode indices are included in column vectors \mathbf{a} , \mathbf{b} , \mathbf{p} and \mathbf{q} .

The details of calculating the T-matrix via DDA is covered in [14], basically involves point-matching the fields (5) with (6). For each combination of mode the indices n and m , we form the corresponding column of the T-matrix out of the solution for the scattering coefficients, p_{nm} and q_{nm} .

5.4. Force and torque

The incoming and outgoing field coefficients are used to calculate the force and torque [15,33] experienced by the rotor at a given point in space. The angular momentum flux divided by the incident power gives the torque efficiency (or normalized torque) about the beam axis:

$$Q_{\tau,z} = \sum_{n=1}^{\infty} \sum_{m=-n}^n m(|a_{nm}|^2 + |b_{nm}|^2 - |q_{nm}|^2 - |p_{nm}|^2) / P_{\text{inc}} \quad (8)$$

in units of \hbar per photon. The coefficients a_{nm} , b_{nm} , p_{nm} and q_{nm} here refer to those for the incoming-outgoing T-matrix formulation whereas the DDA T-matrix uses the incident-scattered formulation. The two types of T-matrices are related by [34]

$$\mathbf{T}^{(\text{in/out})} = 2\mathbf{T}^{(\text{inc/sca})} + \mathbf{I}. \quad (9)$$

It follows that the coefficients can be converted accordingly,

$$\begin{aligned} a_{nm}^{(\text{in})} &= a_{nm}^{(\text{inc})}, \\ b_{nm}^{(\text{in})} &= b_{nm}^{(\text{inc})}, \\ p_{nm}^{(\text{out})} &= 2p_{nm}^{(\text{sca})} + a_{nm}^{(\text{inc})}, \\ q_{nm}^{(\text{out})} &= 2q_{nm}^{(\text{sca})} + b_{nm}^{(\text{inc})}. \end{aligned} \quad (10)$$

The incoming beam power in units of \hbar per photon is

$$P_{\text{in}} = \sum_{n=1}^{\infty} \sum_{m=-n}^n |a_{nm}|^2 + |b_{nm}|^2, \quad (11)$$

and the outgoing power is

$$P_{\text{out}} = \sum_{n=1}^{\infty} \sum_{m=-n}^n |p_{nm}|^2 + |q_{nm}|^2, \quad (12)$$

where a_{nm} and b_{nm} and p_{nm} and q_{nm} are the expansion coefficients for the incoming and outgoing beam, respectively. The absorbed power is simply the difference between incoming power and the outgoing power. However, errors in calculations due to, say, coarse lattice spacings or poorly-converging iteration processes, may introduce an apparent power loss even when the scatterer is supposed to be non-absorbing, in which case, we can compensate for this offset by normalizing against the scattered power instead.

6. Results

6.1. Comparison between the model and the experiment

Our attempts in making the CDR with the intended shape shown in Fig. 8 by two-photon photopolymerization resulted in distortions that caused the structure to resemble a “ring cake” structure (Fig. 1). Whilst the shape of the CDR was not ideal, we were still able to trap and spin it with an LG₀₄ beam. The convergence angle of the beam was 78° and its wavelength was 804 nm in water. From the measured rotation rate of 4 Hz at 20 mW of laser power at the focus, the estimated orbital torque is $0.3 \pm 0.03\hbar$ per photon.

We present the supplementary video material ([Media 1](#)) demonstrating optical trapping and rotation of the rotors. As can be seen from the CCD capture, the rotor is trapped and rotates freely. Although it is difficult to see based on this video that the trapping is three dimensional we have performed additional measurements that verify this by placing a “line” of certain height and moving the rotating CDR over it. We did not see any change in the rotation rate while we performed this measurement. Figure 9 shows the captured frames of the trapped CDR ranging from stationary to rotating at a rate exceeding the 30 Hz frame rate (> 150 mW of beam power) of the CCD camera.

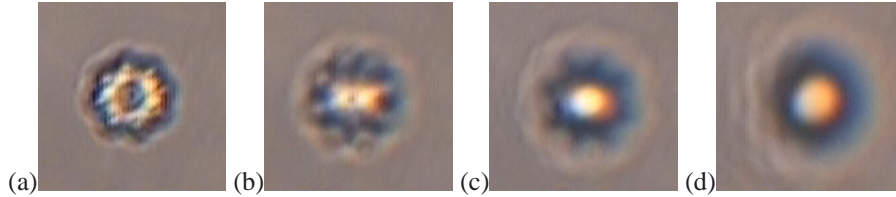


Fig. 9. Video frames of the CDR rotor that is (a) trapped but stationary and being rotated with increasing speeds from (b) to (d). The CCD camera use in the experiment captures at the rate of 30 frames per second. Also see the supplementary video material ([Media 1](#)).

The dimensions of the intended CDR (Fig. 8) were $r_a = 500$ nm, $r_b = 1850$ nm, $h_a = 400$ nm and $h_b = 1400$ nm. To approximate the ring cake shape, we “cropped” the CDR at an imaginary spherical boundary with radius r_b where the origin is the intersection between the rotational axis and its base. The ring cake model is depicted in Fig. 10(a), superimposed with the calculated incident LG₀₄ beam that had a convergence angle of 78°.

We performed force and torque calculations along the beam axis for both the intended CDR and the ring cake; the results are shown in Figs. 11 and 12, respectively. The beam propagates

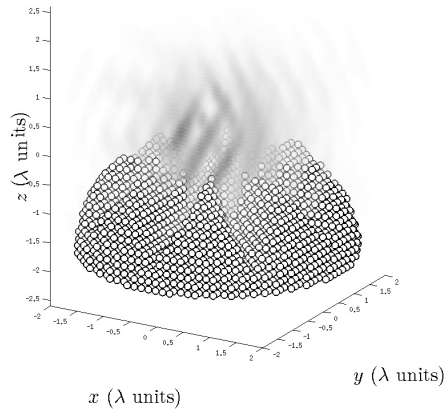


Fig. 10. (a) Ring cake rotor and the incident LG_{04} beam which propagates in the $-z$ direction. The rotor finds equilibrium where its base sits at about -2λ .

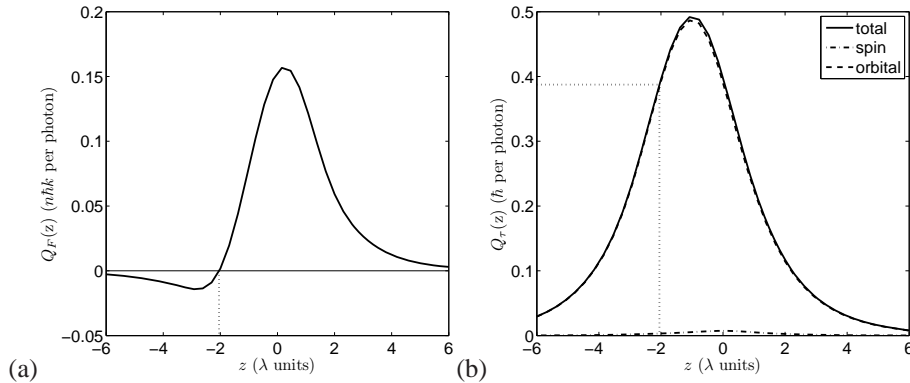


Fig. 11. (a) Force and (b) torque efficiencies versus the displacement of the intended CDR, along the axis of a linearly-polarized LG_{04} trapping beam that propagates in the $-z$ direction. The calculated torque efficiency at equilibrium is approximately $0.39 \hbar$ per photon.

in the $-z$ direction, its linear momentum pushing the rotor away from the focus whilst the gradient forces tries to keep it close to the focus. An equilibrium is reached where the axial force is zero. We take the value of the torque from that equilibrium position. The calculated torques efficiencies for the the CDR and ring cake are 0.39 and $0.28 \hbar$ per photon, respectively. The latter value is closer than that of the experimental measurement of approximately $0.3 \hbar$ per photon. The ring cake was modeled to mimic the shape of the actual fabricated rotor and the discrepancy between the calculated and measured torques is less than 7%.

6.2. Further investigation into Laguerre-Gauss modes

To investigate and confirm the expected optimal azimuthal LG mode for the CDR, we performed the torque calculations at the equilibria for LG_{0l} beams with $l = 0, 1, 2, \dots, 10$. Figure 13 shows the torque efficiencies for both the CDR and the ring cake, where the driving beam convergence angle is kept at 78° . As discussed in section 3, we expected the LG_{04} beam to be

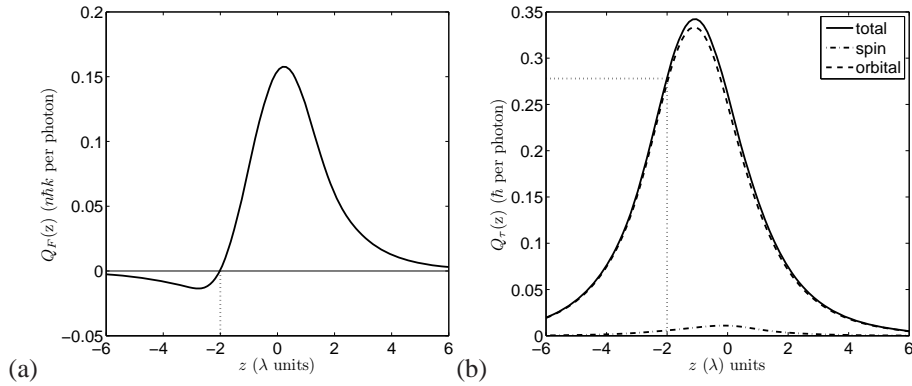


Fig. 12. (a) Force and (b) torque efficiencies versus the displacement of a “ring cake” rotor, along the axis of a linearly-polarized LG₀₄ trapping beam that propagates in the $-z$ direction. The calculated torque efficiency at equilibrium is approximately $0.28 \hbar$ per photon.

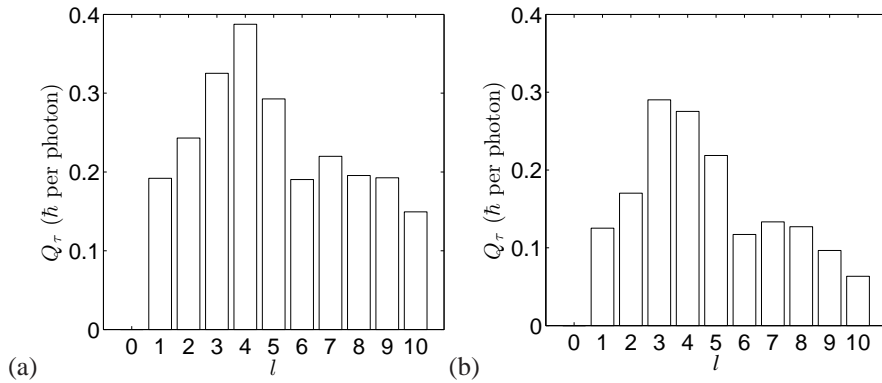


Fig. 13. The calculated torque efficiency versus azimuthal mode l of the (a) CDR and the (b) ring cake rotor, trapped and rotated using linearly-polarized LG_{0 l} beams with the same convergence angle of 78° .

optimal for producing torque. This is indeed the case for the CDR (Fig. 13(a)). However, the results for the ring cake (Fig. 13(b)) show that LG₀₃ produces the highest torque.

We also performed torque calculations of the CDR for LG_{0 l} modes with left-circular, linear and right-circular polarizations. Figure 14(a) shows that, overall, the LG₀₄ beam produces the highest torque. However, in the case where the polarization is left-circular, the LG₀₃ beam produces an approximately equal torque to that from the LG₀₄ beam.

Since the ring size of the LG_{0 l} beam increases with l , it will not illuminate the same part of CDR if the beam convergence angle is kept constant. Thus, we adjusted the beam convergence angle such that the LG donut ring sat at mid-radius (the average of r_a and r_b) of the CDR. Figure 14(b) shows the calculated torque efficiency versus the azimuthal mode l . For this case, where the beam convergence angle is optimal, the LG₀₄ beam produces the highest torques although the value from the linearly-polarized LG₀₅ beam was about equal. The results for $l = 9$ and $l = 10$ were not calculated because their ring sizes cannot be made to fit the mid-radius of the CDR since the physical limit confines the beam convergence angle to less than 90° (or several degrees less in practice).

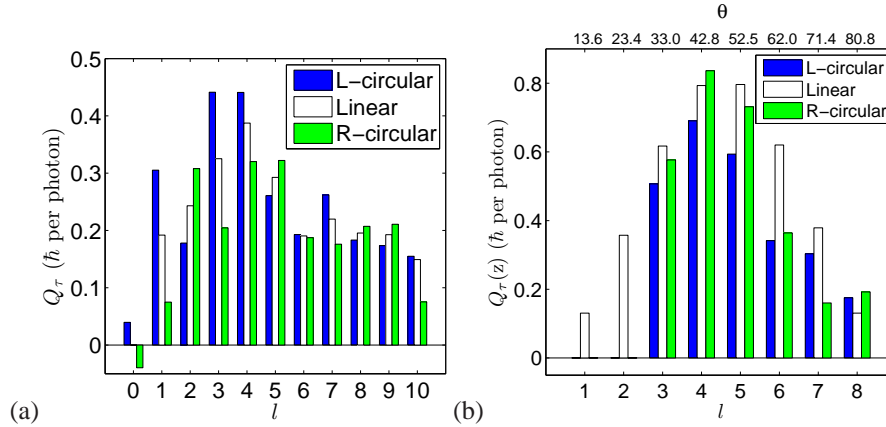


Fig. 14. The calculated torque efficiency versus azimuthal mode l of the CDR for the beam convergence angle θ (a) kept constant at 78° and (b) optimized for each LG_{pl} beam such that the peak intensity of its donut ring coincides with the midway between the inner and outer CDR radii r_a and r_b . The torque values were calculated for incident beams with left-circular, linear and right-circular polarizations.

7. Discussion

Based on the application of Floquet's theorem in the azimuthal direction, described in sections 2 and 3, given that the CDR has 8-fold discrete rotation symmetry, we predicted that the LG_{04} beam should produce optimal torque. While this is true based on the overall results in Figs. 13 and 14, the question remains as to why, under certain conditions, the LG_{03} or the LG_{05} beam produce equal or slightly higher torque than that from the LG_{04} beam.

The LG modes are solutions to the scalar paraxial wave equations where the angular momentum flux is determined by the azimuthal mode l . The VSWF modes, on the other hand, are solutions to the vector Helmholtz equation and the angular momentum is described by the VSWF azimuthal mode m . In the paraxial regime, we expect that the LG_{04} beam would have produced the highest torque. However, we use highly-focused beams in optical trapping where both the spin and orbital angular momentum components of the beam contribute to the orbital torque on the rotor [20]. Further scrutiny of the LG_{03} and LG_{05} beams reveal why they produce the highest torque under certain conditions.

Results from our incident beam calculations are listed in Table 1 which shows the non-zero radial n and azimuthal m VSWF modes for highly convergent ($\theta = 78^\circ$) LG_{0l} beams with left-circular, linear and right-circular polarizations. Here, the only non-zero azimuthal VSWF modes are $m = l \pm 1$. Table 1 also shows that linear polarization is the superposition of left- and right-circular polarizations.

For the LG_{03} beam, the azimuthal mode $m = 4$ exists in the L-circular polarization component. This accounts for the high torque results for the LG_{03} beam in Figs. 13(b) and 14(a). It should be noted that the CDR with 8-fold discrete rotational symmetry also possesses 4-fold symmetry, in which case the azimuthal mode $m = 2$ can provide additional coupling.

In the case of the LG_{05} beam, the R-circular polarization component contains the azimuthal mode $m = 4$. The high torque for this beam can be seen in Fig. 14(b).

Table 1. Radial n and azimuthal modes m with non-zero amplitudes for highly convergent LG_{0l} beams with left-circular, linear and right-circular polarizations.

l	pol.	n	m
3	L-circ.	$4-N_{\max}$	4
3	linear	$2-N_{\max}$	2,4
3	R-circ.	$2-N_{\max}$	2
4	L-circ.	$5-N_{\max}$	5
4	linear	$3-N_{\max}$	3,5
4	R-circ.	$3-N_{\max}$	3
5	L-circ.	$6-N_{\max}$	6
5	linear	$4-N_{\max}$	4,6
5	R-circ.	$4-N_{\max}$	4

8. Conclusion

We performed torque calculations for both the idealized corrugated donut rotor and the distorted ring cake. The latter shape was closer to that of the rotor produced via two-photon photopolymerization and the torque results between the model and experimental measurements we within 7% percent of one another. In the experiment, the LG_{04} was the beam of choice for achieving optimal torque, based on Floquet's theorem that the azimuthal mode of the beam was ideal for a rotor with 8-fold discrete rotational symmetry. Both the experimental and computational modeling results confirmed that to be the case, with a few exceptions.

We also calculated that, depending on the polarization, i.e., left-circular, linear or right-circular, the LG_{03} and LG_{05} beams may produce an equal or slightly higher torque than the LG_{04} beam. This is due to the existence of the VSWF azimuthal mode $m = 4$ in the left-circular and right-circular polarization components in highly converging LG_{03} and LG_{05} beams, respectively.

The DDA T-matrix method proves its usefulness as a modeling method for repeated calculations with varying relative positions and illumination of arbitrarily-shaped objects. Thus, it is particularly suitable for providing aid in prototyping optically-driven micromachines. The modeling results provide insight for achieving optimal design for microrotors and also to select the beam parameters most suited for a particular rotor geometry.

In contrast with the rotor with a tall stalk [7], the compact and relatively flat structure of the CDR is better suited for lab-on-a-chip applications where it can function as a pump or a mixer. It could also be fabricated via large-scale conventional photolithography or a similar process. Moreover, the ring-shape of the CDR is compatible with LG beams in that it can be stably trapped in 3D and it is able to exploit the OAM of the beam. If need be, the CDR can also be secured in place with an axle.

Acknowledgments

This work was supported by the Australian Research Council grant number DP1095880.